CARBON 86 (2015) 69–77

Available at www.sciencedirect.com

ScienceDirect

journal homepage: www.elsevier.com/locate/carbon

Biaxial compressive behavior of embedded monolayer graphene inside flexible poly (methyl methacrylate) matrix

Guorui Wang [a,b], Luqi Liu [a,*], Zhaohe Dai [a,c], Qing Liu [a,c], Hong Miao [b], Zhong Zhang [a,*]

[a] National Center for Nanoscience and Technology, Beijing 100190, PR China
[b] Department of Modern Mechanics, University of Science and Technology of China, Hefei 230026, PR China
[c] University of Chinese Academy of Science, Beijing 100049, PR China

ARTICLE INFO

Article history:
Received 9 October 2014
Accepted 13 January 2015
Available online 20 January 2015

ABSTRACT

We systematically investigated the in-plane biaxial compression behavior of the monolayer poly (methyl methacrylate) (PMMA)/graphene/PMMA system by in situ Raman spectroscopy. The shifts of Raman G-band peak position exhibited three-stage features with increasing compressive strain, including elastic deformation, local Euler-buckling and continuous compression. Our results demonstrated that the mechanical stability of graphene based flexible electrodes greatly depended on the deformation modes, applied strain level and interfacial adhesion. The embedded graphene sheets performed reversible compressibility at lower strain level over many cycles. With further increasing compressive strain, the strain distribution of the embedded graphene sheet turned non-uniform, and the interfacial debonding occurred. An analytical model based on the mechanical instability theory was proposed to depict the interfacial debonding behavior of individual graphene sheet, which agreed well with the experimental results.

1. Introduction

Stretchable and flexible electronics have drawn great attention over the past decade due to their good flexibility, lightweight, transplantable, and portable capabilities. To meet various desires required by flexible electronics, many alternative transparent electrodes have been developed to replace commercially available indium tin oxide (ITO) electrodes, and materials used include metal grids [1], metallic nanowires [2], conductive polymers [3], and carbon nanotubes (CNTs) [4,5]. Recently, the discovery of graphene brought a new alternative to conventional ITO electrodes due to its unique combination of extraordinary electrical, optical and mechanical properties [6]. Many research groups have demonstrated the resilience of graphene based flexible electrodes as a promising candidate in a wide range of applications, such as field effect transistors (FETs), solar cells, organic light-emitting diodes (OLEDs), touch screens, and electrochemical sensors [7–9]. Apart from the high electrical, optical performance as required by flexible opto-electronic devices, the mechanical stability of electrodes and recoverability under deformation were major factors to determine the device stability and durability. Various mechanical deformations such as tension, bending, and twisting would apply to the device under the various harsh working conditions during the fabrication, assembling, and manipulation processes. The

* *Corresponding authors:* Fax: +86 10 6265 6765 (L. Liu), +86 10 8254 5586 (Z. Zhang).
E-mail addresses: liulq@nanoctr.cn (L. Liu), zhong.zhang@nanoctr.cn (Z. Zhang).
http://dx.doi.org/10.1016/j.carbon.2015.01.022
0008-6223/

occurrence of mechanical failure (e.g. interfacial delamination) could severely deteriorate the performance and reliability of device when the desired properties of the flexible devices are proposed to be tunable through reversible and repeatable mechanical manipulation [10,11]. Therefore, it is crucially important to monitor the mechanical responses of flexible electrodes under various stress states, evaluate the interface stability and recoverability, clarify the possible failure modes as well as the limit of strain-induced irreversible structure deformation.

As determined by the stiffness of substrates, electrodes as well as their microstructure features, the mechanical design is generally required for the flexible electrodes to fulfill the desired properties when subjected to repeatable mechanical manipulation. For example, the wrinkled, rippled and/or crumpled microstructure features were introduced to graphene based rubbery electrodes to endow it with good recoverability under cyclic mechanical stretching [12]. However, from the viewpoint of the mechanical stability of graphene based flexible electrodes, earlier works have concentrated on the loading role of monolayer or few-layer graphene sheets carried, interfacial shear stress, and the possible deformation mode of the graphene sheets under tensile and compressive mode [13–16]. For example, Young et al. monitored the strain distribution of the embedded graphene inside PMMA beam under tensile deformation. The experimental data indicated that strain distribution was relatively uniform at low applied strain levels, but became highly non-uniform above certain strain level due to the crack propagation of the resin layer [17]. Later, Galiotis and coworkers investigated in detail both stress uptake and buckling strain of embedded graphene under compressive deformation. The critical buckling strain was found to be greatly dependent on the length to width ratios (l/w) of individual graphene platelets, and a permanent wrinkle was formed after cyclic deformation [18]. In addition, theoretical simulation based on coarse-grain model has predicted the possible buckling deformation of the embedded graphene under compression, and found that the buckling mode greatly depends on the adhesion strength and effective stiffness of graphene and substrate [19]. It should be noted, however, that the mechanical mode aforementioned is relatively simple, and it is not comparable to the deformation states of flexible electrodes suffered in reality. In general, for thin solid film based flexible electrodes, the stress states of the embedded graphene platelet suffered at least come from biaxial directions.

Raman spectroscopy is an inelastic photo scattering spectrum, which reflects unique information concerning the vibration and electronic properties of materials. It has become a powerful technique to identify the structures of carbon materials such as the diameter and distribution of carbon nanotubes, their metallic or semiconducting nature, the number of graphene layers, and the crystallographic orientation of graphene [20–23]. Furthermore, due to the high sensitivity to shift-induced symmetry, the non-destructive quality, and the ability to be used in micro-analytical studies, Raman spectroscopy has been successfully utilized to unravel microstructure deformation of carbon materials suffered under the external loads [24,25].

To reveal the mechanical response and evaluate mechanical stability of the embedded graphene inside plastic matrix, herein, we systematically investigated the mechanical deformation of the embedded graphene when subjected to in-plane biaxial compression as induced by thermal shrinkage method. The compressive deformation modes of the embedded graphene sheets were monitored by in situ micro-Raman spectroscopy. Interestingly, unusual three stages of mechanical deformation were observed during compression process: namely, elastic deformation, local Euler-type buckling, and continuous compression. On the basis of the shifts of specific Raman band, we calculated the compressive stress acting on the individual graphene sheets, estimated the effective flexural rigidity of the embedded graphene, and demonstrated a permanent and irreversible interfacial debonding behavior occurred in the graphene–PMMA system. Furthermore, a simplified model to predict the critical interface debonding compression strain was proposed and fitted well with the experimental data. Our results will be beneficial to the design of graphene based flexible devices with excellent mechanical stability and durability, and open up the possibility of utilizing strain engineering to improve devices performance.

2. Experimental methods

The graphene samples were prepared by micromechanical cleavage [26] and adhered to Si wafer substrate with a 300 nm SiO_2 capping layer. Optical microscopy was used to locate the graphene sheet and the thickness was further confirmed by Raman spectroscopy. A thin layer of PMMA (2 wt.% in chloroform) was spin-coated on the substrate prior to the transfer [6,27]. Afterwards the detachment of the PMMA–graphene layer from the initial surface was done by partially etching the surface of SiO_2 with a 1 M NaOH aqueous solution. As a result, a PMMA membrane with all of the graphite/graphene sheets attached to it was obtained. Finally, this membrane was laid over the target substrate of PMMA with the localization of graphene sheets as Alfonso Reina explained [22]. The detailed procedures were plotted in Fig. 1 and three prepared samples were shown in Supporting information S1 including their optical images as well as Raman spectra in the full spectral range.

The Raman spectra were obtained with a Renishaw Raman spectroscope, using the 514 nm line of an Ar laser, equipped with a Linkam cooling cell. The temperatures in our experiments ran from 60 down to −150 °C by liquid nitrogen as the cooling agent in the cooling cell, while liquid helium was further employed to introduce larger compressive strains to the embedded graphene that was placed in a liquid helium pot, when the ambient temperature was reduced to −263 °C (10 K). Here the temperature at 60 °C was selected as a reference based on the fact that the thermal stress of embedded graphene maintained during the curing process could be entirely released. Thermal equilibrium in each case was reached by holding the specimen for 3–5 min at constant temperature. The Raman spectrum was taken at a minimum of three points in the central area of graphene flake at a certain temperature. All bands in the Raman spectra of graphene were fitted with Lorentzians. To obtain the Raman images,

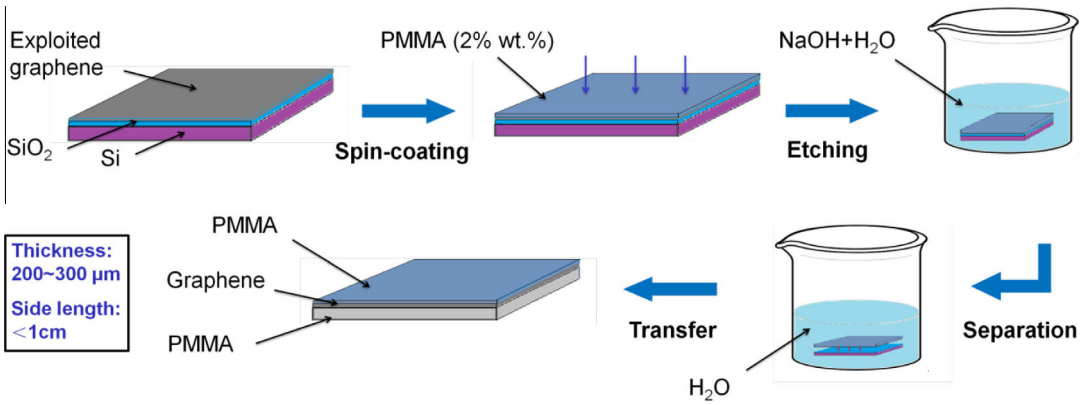

Fig. 1 – Schematic illustration of procedures of sample preparation. (A color version of this figure can be viewed online.)

the sample was moved with a step size of 300 nm and Raman spectra from every spot of the sample were recorded. Raman images were constructed using a parameter such as peak frequency and peak intensity by using WIRE Project software.

The sketch of the in-plane biaxial compression applied to graphene was performed by molecular dynamics simulation. The compressive strains were applied to a square graphene with a size of $10.0 \times 10.0\ nm^2$ in both length and width directions using periodic conditions.

3. Results and discussion

Fig. 2a and b show the typical optical and Raman images of graphene flakes embedded inside PMMA matrix as prepared by mechanical cleavage of natural graphite. Apparently, the different contrast regions in Fig. 2a are related to flakes with different numbers of graphene layers, which are consistent with the image of Raman G-band in Fig. 2b. Fig. 2c illustrates the variation in Raman G-band intensity with different numbers of graphene layers. In this work, we mainly focus on the compressive behavior of monolayer graphene sheet embedded inside PMMA matrix.

In general, thermal stress would be introduced to a structure or material to constrain against expansion or contraction as the environmental temperature changes [28]. For PMMA/graphene/PMMA systems, the thermal stress acting on graphene comes from the differences in coefficients of thermal expansion (CTE) between graphene sheets and PMMA matrix. Besides, the magnitude of thermal stress is also influenced by the differences in the elastic modulus between the two components and the temperature gradient of the systems. During the cooling process, the compressive strain for the PMMA/graphene/PMMA systems can be inferred from the following Eq. (1) according to the classical elasticity theory [29]:

$$\varepsilon = \left(\alpha_{substrate} - \alpha_{graphene}\right)\Delta T \tag{1}$$

where $\Delta T = T - 60$ is the temperature gradient, with 60 °C as the reference temperature, $\alpha_{substrate} = (68 \pm 2.0) \times 10^{-6} K^{-1}$ [30,31] and $\alpha_{graphene} = (-8.0 \pm 0.7) \times 10^{-6} K^{-1}$ [32] are the CTE of the matrix and graphene, respectively. Herein, it is worth noting that the compressive stress of the embedded graphene is quite different from that of embedded CNT fiber reported earlier in our work, in which the thermal stress mainly caused the compression along the fiber axis during the cooling process due to one-dimensional structure feature [28]. Instead, a biaxial state of compressive stress rather than uniaxial stress was applied to the embedded graphene as the temperature decreased, as depicted in Fig. 3. Therefore, in order to simulate and reveal the deformation modes of the embedded graphene in the real conditions, using the thermal shrinkage approach to perform compressive deformation is desirable.

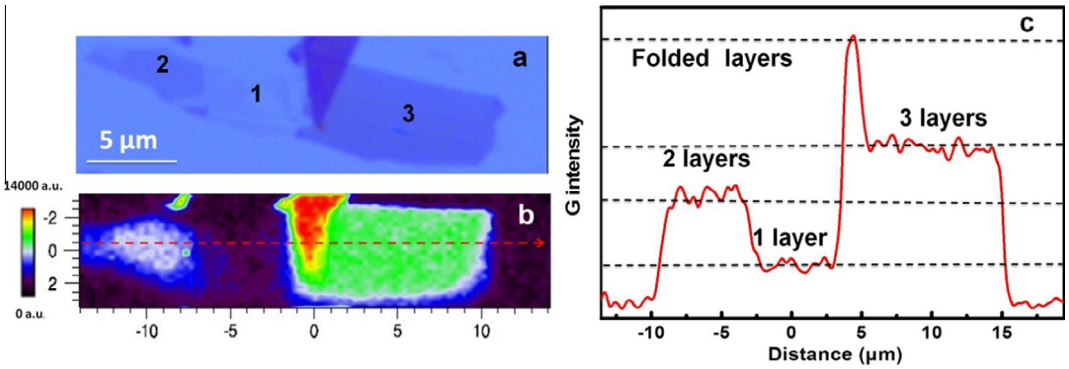

Fig. 2 – (a) Optical micrograph of graphene flakes containing monolayer (sample #2), bilayer, and trilayer regions. (b) Raman image of graphene flakes plotted by the intensity of Raman G-band. (c) The intensity cross-section of the Raman image corresponding to the dash line in (b). (A color version of this figure can be viewed online.)

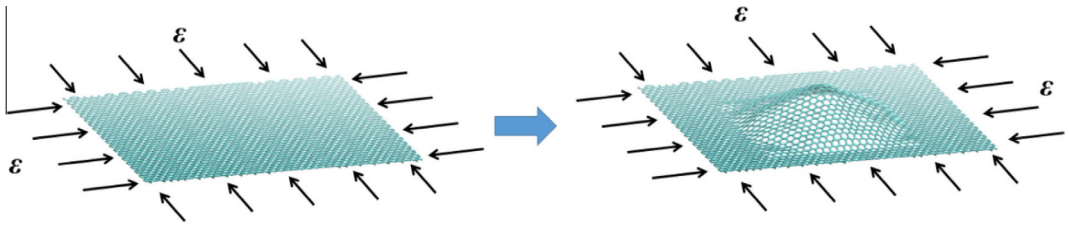

Fig. 3 – The sketch of the in-plane biaxial compression applied to graphene by molecular dynamics simulation. (A color version of this figure can be viewed online.)

Considering the fact that specific Raman band is sensitive to variations in interatomic distances in specimens, micro-Raman spectroscopy was hence employed to investigate the compressive deformation of the embedded graphene inside PMMA matrix. The shift of Raman G-band under compression enables us to estimate the compressive deformation as well as the apparent compressive mechanical behavior of the embedded graphene. Moreover, based on the shifted trend of Raman G-band, the deformation mechanism of graphene could also be inferred. Fig. 4a presents the typical Raman G-band of monolayer graphene embedded inside PMMA matrix at various temperatures ranging from 60 to −150 °C. Apparently, the upward shifts of Raman G-band can be observed with decreasing temperature, which is approximately 15 cm^{-1} shift. The apparent upward shifted trends are expected, and arise from the shortening of the C=C bond length of graphene sheets as a result of the applied compressive deformation. Specifically, accompanying the continuous reduction of temperature, the shifts of Raman G-band peak position exhibit three-stage features, as shown in Fig. 4b: initially, the Raman G-band increases linearly with decreasing temperature; once the temperature exceeds a certain point (~−50 °C), the Raman G-band reach a plateau region; after that, Raman G-band appears a sluggish up-shifted tendency with further decrements of temperature down to −150 °C. According to the work that has reported the negligible effects of temperature changing on Raman G-band shifting of the graphene sheet, the Raman shifts in our experiment are supposed to be determined by the thermal induced compression [33]. Thus, the variation of Raman G-band is related directly to the microstructure deformation of the embedded graphene when subjected to external compression. Through monitoring the compressive deformation of the embedded graphene, the load-bearing status, deformation mechanism, its mechanical stability and recoverability of the embedded graphene can be derived. We will discuss them from the following three parts.

3.1. *Stage-I, elastic deformation*

In the earlier strain region as shown in Fig. 5, up to approximately −0.6% strain, the graphene sheet appears elastic and reversible compressive behavior. The shift of Raman G-band increases linearly with applied compressive strain with shift rate $\left(\frac{\partial\omega_G}{\partial\varepsilon}\right)$ in the range of ~12.1 cm^{-1}/% (sample #3) to ~15.6 cm^{-1}/% (sample #2), and no apparent G-band splitting is observed. The obvious difference in shift rate could be attributed to the variation in flake sizes as well as residual strain. Compared to the shift rate of ~10.8 cm^{-1}/% and ~31.7 cm^{-1}/% for the G^+ and G^- mode under compression respectively [18], the apparent difference could be related to the different compression modes (uniaxial versus biaxial), varied lateral dimensions of graphene flakes and different interfacial adhesion [18,34]. Moreover, the low shift rate derived in the current work further implies that the compressive strain of individual graphene sheet deformed is lower than the applied strain levels. Thus, we speculate that the electronic structure of graphene sheet would maintain under

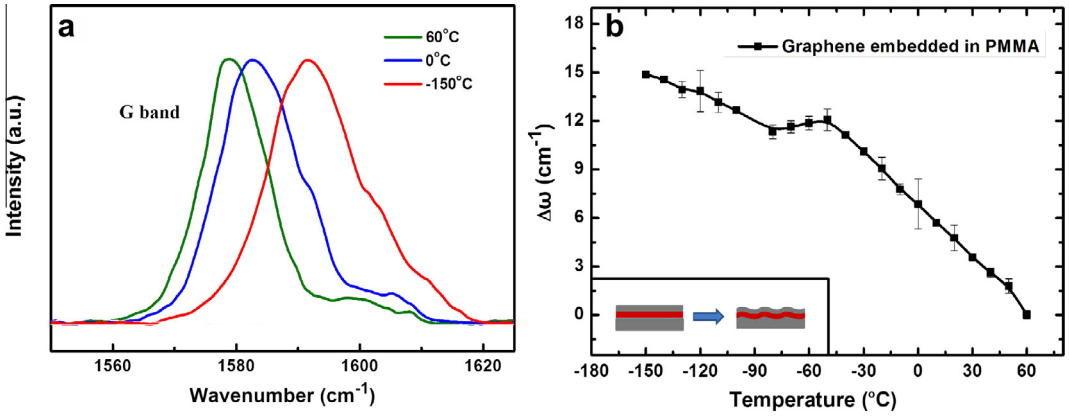

Fig. 4 – (a) Variations of Raman G-band spectra of the embedded graphene monolayer at various temperatures. (b) The shift of Raman G-band as a function of applied temperatures referred 60 °C, and schematic diagram of the local Euler-buckling occurrence of graphene sheet (insert). (A color version of this figure can be viewed online.)

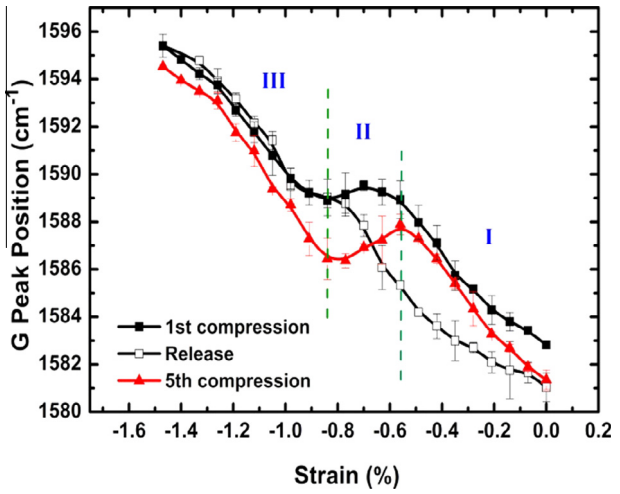

Fig. 5 – Raman G-band versus strain over a compression/relaxation cycle. (A color version of this figure can be viewed online.)

low biaxial compressive deformation. It was further supported by Ni's work, in which they stated that the uniaxial strain would affect the electronic properties of graphene much more significantly [16].

In addition, the Raman shifts of graphene in the stressed state enables us to estimate the apparent mechanical behavior of the embedded graphene sheet. Considering the elastic deformation of graphene experienced, the biaxial compressive stress acting on graphene sheet is calculated based on elastic theory [35,36]. The detailed procedure is shown in Supporting information S2 and the stress can be finally inferred from Eq. (2):

$$\sigma = \frac{\omega_0(\omega_\sigma - \omega_0)}{A(S_{11} + S_{22})} \tag{2}$$

where ω_σ and ω_0 are the frequencies of Raman G-band under stressed and unstressed conditions, A is the phenomenological coefficient, S_{11} and S_{22} are compliance coefficients. Using $A = \omega_0 \frac{\partial \omega_\sigma}{\partial \varepsilon}$ and $S_{11} = 0.98 \times 10^{-12}$ Pa^{-1} and $S_{12} = -0.16 \times 10^{-12}$ Pa^{-1}, and $\omega_0 = 1580$ cm^{-1}, the stress of individual graphene sheets carried can be derived [37]. The derived data shown in Fig. S4 presents that the compressive stress acting on the graphene monolayer could reach as high as ~6 GPa at the strain level of ~−0.6%. Such extraordinary load-bearing capability of monolayer graphene sheet further sheds light on the potential in composites. Also, we predict that graphene based flexible electronics could exhibit excellent creep-resistance behavior in practical application, and it will be beneficial to extend stability and durability of flexible electronic devices under external loads [38].

3.2. *Stage-II, local Euler-type buckling*

Once the compressive strain exceeds a certain point, Raman G-band reaches a plateau region shown in Fig. 5, and the localized Euler-type buckling occurs as illustrated in the inset in Fig. 4b. The compressive strain that caused the initiation of local Euler-type instability is on the level of ~−0.8%. Considering its atomic level thickness and high flexibility, the graphene platelets could be compressed continuously without permanent structure deformation. Thus, on the basis of mechanical instability theory, we could explore the influence of the graphene lateral dimensions on the initiation of local Euler-type buckling as well as the critical buckling strain in more detail. Herein, we compare the compressive behaviors of three individual graphene monolayers with different lateral dimensions. As seen, the three-stage compressive behaviors are observed for all testing samples (Supporting information S3). Table 1 summarizes the detailed information of the three samples as well as the critical local buckling strain ($\varepsilon_{buckling}$) derived from Fig. S5. It can be inferred that the $\varepsilon_{buckling}$ is affected by not only the l/w ratio (comparing sample #1 and #2) but also the absolute dimension value (comparing sample #1 and #3). Herein, a geometric term k is introduced to interpret the size effect, which lies in the size dimension combined with the numbers of half-waves where the flake buckles along the strain axis as represented in Eq. (3) [39]:

$$k = \frac{m^2}{l^2} + \frac{n^2}{w^2} \tag{3}$$

where l is the length and w is the width of graphene sheet, m is the number of half-waves in the length direction and n is the number in the width direction. For example, for sample #1, where length $l = 4$ μm and width $w = 2$ μm, two and one half-waves are expected to occur along length and width directions, respectively, and thus $k = 0.5$. In contrast, for sample #3 with length 8 μm and width 4 μm, and hence the same amount of half-waves occurring, the corresponding term $k = 0.125$. Therefore, it is clear that even with the equal l/w value, the variation in lateral dimensions will lead to distinct size effects, which is confirmed by the different $\varepsilon_{buckling}$ as shown in Table 1. If we plot the k as a function of $\varepsilon_{buckling}$, a linear relation is obtained as shown in Fig. S6, in which $\varepsilon_{buckling}$ reduces as k falls off.

Theoretically, $\varepsilon_{buckling}$ of a rectangular thin shell under biaxial compression is given by Eq. (4) [39]:

$$\varepsilon_{buckling} = k\frac{D\pi^2}{C} \tag{4}$$

where D and C are the flexural and tension rigidities of materials, respectively. For a given material, the $\frac{D\pi^2}{C}$ term is treated as a constant as depicted by the slope of the fitting line in Fig. S6. There is a linear relation between the k and $\varepsilon_{buckling}$. Consequently, the apparent flexural rigidity of the embedded graphene sheet could be derived experimentally (see Supporting information S3), which is 6 orders of magnitude higher than that of suspended graphene. Compared with the result of Frank's work where apparent flexural rigidity of embedded

Table 1 – Size, number of half-waves, geometrical terms k, critical local Euler-buckling strain and $\frac{\partial \omega_G}{\partial \varepsilon}$ values of the studied graphene flakes.

Sample	Size (μm)	m	n	k (/μm^2)	Critical strain
1	2 × 4	1	2	0.5	−0.9%
2	5 × 3	2	1	0.27	−0.8%
3	4 × 8	1	2	0.125	−0.7%

graphene was estimated to 12 MPa μm^3 [18], while it is approximate to 8.4 MPa μm^3 here. Similarly, both of them are 6 orders of magnitude higher than that of suspended graphene, implying the effect of lateral support offered by polymer matrix. Meanwhile, the slight difference between these two values might be due to distinct material systems. In our work, graphene is entirely embedded in PMMA instead of being embedded in PMMA and SU8 or S1805 on either of the graphene's surfaces. It is noting that the obtained apparent flexural rigidity is only an approximation by linear fitting, which is inevitably subjected to errors. With various sizes of graphene sheets including extreme cases (e.g. $l \gg w$) [18], a nonlinear behavior might be expected. In spite of this, the considerably high flexural rigidity demonstrates that surrounding polymer matrix could provide a dramatic improvement to its compression behavior and it has an inspired significance to improve the stability of flexible electrodes.

3.3. *Stage-III, continuous compression*

The graphene sheets could be continuously compressed with further increasing compressive strain, as evidenced by a sluggish up-shifted trend (~−10.4 cm^{-1}/%) of Raman G-band position. This unusual phenomenon implies that the graphene sheet in our experiments could continuously carry the external loads without permanent failure, whereas the irreversible collapse at interfacial regions occurred under uniaxial compression in the reference [18,34]. We suggest that the excellent compressibility of the PMMA/graphene/PMMA system at large applied compressive strain could be attributed to the excellent interfacial stability and the different deformation modes. Tsoukleri et al. reported the occurrence of the irreversible interface failure occurred as the compressive strain was up to ~0.7% for the PMMA/graphene/SU8 photoresist system [34]. The brittle feature of the SU8 photoresist resulting from its intrinsic three-dimensional network-like structure would greatly inhibit the interface stability of graphene based electrodes at large applied compressive strain, in which the cracks easily formed at the SU8 layer. Instead, PMMA with linear structure feature behaved excellent plastic characteristics under deformation, and thereby no apparent interfacial failure was observed in our system.

Additionally, the recoverability of graphene based electrodes is an important issue to affect the mechanical stability of graphene based flexible devices when subjected to repeatable mechanical manipulation. As stated earlier, the interfacial adhesion and deformation mode would greatly affect the mechanical stability of the graphene based flexible electrodes [27,40]. In order to confirm the mechanical recoverability of the embedded graphene sheets, we further conduct the cyclic compression/relaxation tests through controlling temperature procedures as illustrated in Fig. 5. In the first-cycle compressive deformation with strain up to 1.5%, the mechanical behavior of embedded graphene platelet is similar to that shown in Fig. 4b. After that, with the increase of temperature accompanying by the relaxation of both matrix and graphene sheet, the Raman G-band shows apparent down-ward shifts, indicating the relaxation of the compressed C=C bond of graphene. Moreover, the shifted trend of the Raman G-band along unloading part is slightly different from that along the loading one. Specifically, no apparent plateau region is observed during the unloading process due to the slow recovery of the buckled graphene sheets. But the shifted rates of the Raman G-band for Stage-I and Stage-III are kept consistent during the loading/unloading process, with the slopes ~12.2 cm^{-1}/% and ~11.9 cm^{-1}/% in loading and ~13.1 cm^{-1}/% and ~12.4 cm^{-1}/% in unloading, respectively. After five-cycle loading/unloading treatment, the shifted trends of the Raman G-band in Stage-I and Stage-III still keep the similar constants as the initial one, implying the good recoverability of the embedded graphene sheet. But it is worth noting that the initiation of local Euler-type buckling slightly shifts to low compressive strain level due to the repetitive loading/unloading treatment induced weaker interfacial adhesion.

Aforementioned, the recoverability of graphene sheet under mechanical deformation is an important issue to determine the device stability and durability. Experimentally, we have demonstrated the excellent mechanical recoverability of the PMMA/graphene/PMMA system when subjected to repetitive compression with strain limit up to 1.6%. To further explore the deformation process and clarify the possible fracture mechanism of the embedded graphene sheets, herein, we increased the compressive strain level up to ~2.3% by using liquid He as cooling agent. Given that strain-induced shift of the Raman 2D-band of monolayer graphene platelet is twice larger than that of the Raman G-band under tensile/compression deformation [41], therefore, we utilized Raman 2D-band to reveal the strain distribution of the embedded graphene sheets before and after mechanical treatment. Fig. 6a shows the Raman 2D-band image mapping of the monolayer graphene sheet experienced the apparently residual compressive stress resulting from the sample preparation process. As seen, the residual compressive strain of the embedded graphene sheet is roughly uniformly distributed within the whole area (sample size 3 μm × 5 μm) with slight variation as indicated by arrows. Considering that a piezo stage with a step size of ~300 nm and a Raman spectrum was recorded at every point, thus, we attribute the variation in strain distribution to the wrinkled feature of the graphene sheets during sample fabrication process [34]. After mechanical loading/unloading treatment with maximum compressive strain up to ~2.3%, we could see that the strain distribution of the graphene sheet turns highly non-uniform as shown in Fig. 6b indicated by solid-line circle. The center part in the sheet suffers apparently residual compressive strain as compared with its neighboring parts. To confirm the occurrence of permanent deformation at the interfacial region under large applied compressive strain levels, herein, we further applied biaxial compression to the sample and investigated the shift rate of Raman G-band in specific Region A and Region B. The corresponding Raman spectrum is presented in Supporting information S4. Apparently, in Fig. 6c, the Region B displays typical three-stage features with shift rate of −13.3 cm^{-1}/% (Stage-I), −12.1 cm^{-1}/% (Stage-III) respectively. The shifted rates are close to that in Fig. 5, further indicating the excellent recoverability of the localized graphene sheets under mechanical deformation. Whereas the shifted trend of Raman G-band in Region A is quite different from that in Region B, where the shift rate (Stage-I) decreases to −9.1 cm^{-1}/% as compared to that in Region B

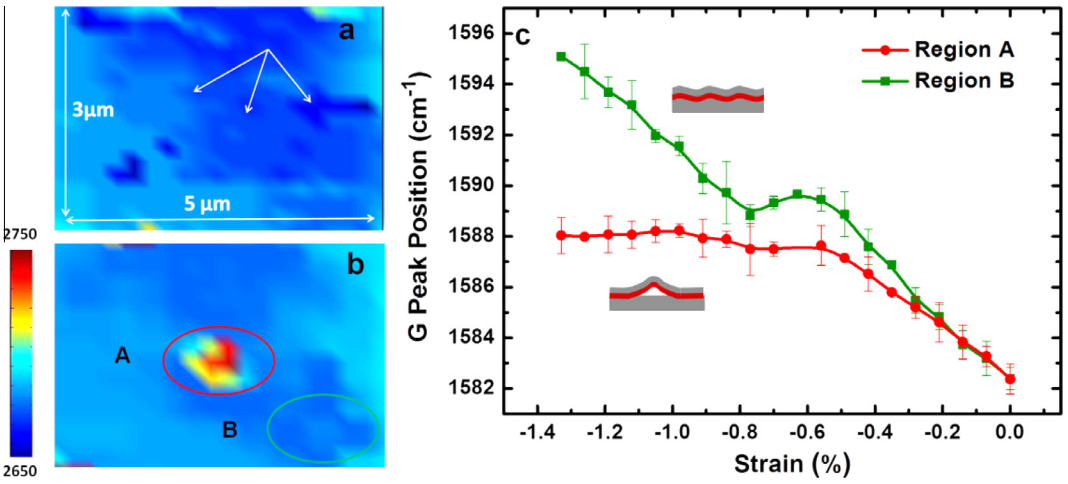

Fig. 6 – Raman image of monolayer graphene plotted by the peak position of Raman 2D-band (a) before and (b) after the large compressive deformation. (c) Peak position of Raman G-band as a function of strain for the two regions as presented by circles in (b). (A color version of this figure can be viewed online.)

(−13.3 cm^{-1}/%), and no further G-band shift is observed after reaching plateau region (∼−0.6%). We speculate the ignition of interfacial debonding once the strain level reaches ∼−2.3%. After that, the strong interfacial adhesion turns weak. Consequently, the weaken interfacial adhesion in Region A leads to poor interfacial shear-stress-transfer efficiency, and eventually the interfacial debonding occurs at relative low strain level in the PMMA/graphene/PMMA system. Expectedly, such areas would act as stress concentration sites to induce interfacial delamination when subjected to further mechanical manipulation. Therefore, it is practically important to monitor the strain distribution of the embedded graphene sheet to ensure its stability and durability once utilized as flexible electrodes. Additionally, the amplitudes of mechanical manipulation, interfacial adhesion, and deformation modes are all important parameters to determine the mechanical stability and durability of graphene based flexible electrodes.

To deeply understand the interfacial debonding behavior in typical graphene-polymer systems as presented in Fig. 6b, we propose a theoretical model by simplifying two-dimensional graphene sheet as a one-dimensional bent beam based on the mechanical instability theory as depicted in Fig. 7a. Considering the wrinkled nature of suspended graphene sheet, the embedded graphene sheet would still maintain such wrinkled morphology within polymeric matrix [42,43]. Herein, we presume that part of the embedded graphene sheet sustains the initially wrinkled morphology with relatively strong interfacial interaction as identified by AB part in Fig. 7b, while the other part exhibits flat morphology with relative weak interfacial adhesion identified by BC part. As expected, when subjected to mechanical manipulation, the interfacial debonding would initiate at areas with weak adhesion and then propagate to the areas with strong adhesion, eventually lead to the interfacial delamination. Thus, the strain level applied to the graphene-polymer system to induce mechanical debonding is a critical factor to affect the mechanical stability of graphene based flexible electrodes. In this work, we define the critical stain ($\varepsilon_{buckling}$) to predicate the interfacial debonding in the PMMA/graphene/PMMA system with weak adhesion under compression as represented by Eq. (5). Detailed information can be seen in Supporting information S5.

$$\varepsilon_{debonding} = \frac{\pi^2}{\varphi^2 \sin\frac{\varphi}{2}}\left(\varphi\cos^2\frac{\varphi}{2} + \frac{\varphi}{2} - \frac{3}{2}\sin\varphi\right) \quad (5)$$

where φ is the central angle of the AB part. The values of φ ranged from 9.3° to 22.8° in the reference [44,45], and thus the calculated $\varepsilon_{debonding}$ is in the range of −0.4% to −2.2%, in which the large value implies strong interfacial adhesion while the low value corresponds to poor interfacial adhesion. Experimentally, the derived $\varepsilon_{debonding} \sim -0.6\%$ from Fig. 6c and ∼−0.5% from Fig. S10, are consistent well with the analysis model in Fig. 7e, implying that the interfacial debonding initiated from the weak interface region. Additionally, for the graphene-polymer system with strong interfacial adhesion, the interface adhesion would turn weak once the strain beyond certain limit as shown in Fig. 6a and b. Therefore, the critical debonding strain is an important parameter to guide the mechanical manipulation of graphene based flexible electrodes with various interfacial adhesion.

4. Conclusion

With the help of in situ micro-Raman spectroscopy, we systematically investigate the mechanical properties and its microstructure evolution of the individual graphene sheet inside flexible PMMA matrix when subjected to in-plane biaxial compression deformation. Different from the results in the literatures, our results demonstrated that the graphene could continuously carry compressive loads without permanent failure even after critical local Euler-type buckling strain (∼−0.8%). The graphene–PMMA system exhibits outstanding mechanical recoverability after many cyclic loading and unloading treatments at relative low strain level. However, with continuously increasing compressive strain up to

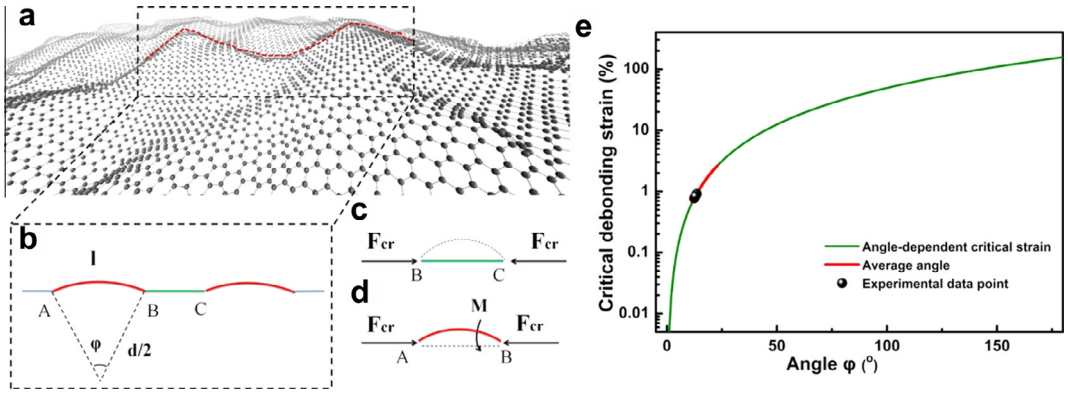

Fig. 7 – (a) Randomly wrinkled graphene sheet by molecular dynamics simulation. (b) Two-dimensional graphene sheet was simplified as one-dimensional bent beam which consists of (c) the weak interface part BC and (d) the initial wrinkled part AB with radius *d*/2 and central angle φ. (e) Plot of central angle (φ) of wrinkled graphene sheets shown in Fig. 5b versus critical debonding strain ($\varepsilon_{debonding}$). (A color version of this figure can be viewed online.)

~2.3%, the interfacial areas turned weak, and eventually, the interfacial debonding occurred at some areas with weak interfacial adhesion as evidenced in our work. The theoretical analysis based on mechanical instability theory indicated that critical debonding strain was in the range of −0.4% to −2.2%, which agreed well with our experimental data. Beyond that, combining the excellent effective flexural rigidity and remarkable compressive stress of the compressed graphene sheet, our work demonstrated the excellent reinforcing role of graphene played in the flexible electronics. It will be helpful not only to guide the design of graphene based flexible electronics with excellent mechanical stability and durability, but also to deeply understand the deformation modes of various nanofillers based flexible electronic devices.

Acknowledgement

This project was jointly supported by the National Key Basic Research Program of China (Grant Nos. 2012CB937503 and 2013CB934203) and the National Natural Science Foundation of China (Grant Nos. 51173030 and 11225210).

Appendix A. Supplementary data

Supplementary data associated with this article can be found, in the online version, at http://dx.doi.org/10.1016/j.carbon.2015.01.022.

REFERENCES

[1] Kang MG, Kim MS, Kim J, Guo LJ. Organic solar cells using nanoimprinted transparent metal electrodes. Adv Mater 2008;20(23):4408–13.
[2] Lee J-Y, Connor ST, Cui Y, Peumans P. Solution-processed metal nanowire mesh transparent electrodes. Nano Lett 2008;8(2):689–92.
[3] Kim YH, Sachse C, Machala ML, May C, Müller-Meskamp L, Leo K. Highly conductive PEDOT: PSS electrode with optimized solvent and thermal post-treatment for ITO-free organic solar cells. Adv Funct Mater 2011;21(6):1076–81.
[4] Niu C, Sichel EK, Hoch R, Moy D, Tennent H. High power electrochemical capacitors based on carbon nanotube electrodes. Appl Phys Lett 1997;70(11):1480–2.
[5] Rowell MW, Topinka MA, McGehee MD, Prall H-J, Dennler G, Sariciftci NS, et al. Organic solar cells with carbon nanotube network electrodes. Appl Phys Lett 2006;88(23):233506.
[6] De Arco L Gomez, Zhang Y, Schlenker CW, Ryu K, Thompson ME, Zhou C. Continuous, highly flexible, and transparent graphene films by chemical vapor deposition for organic photovoltaics. ACS Nano 2010;4(5):2865–73.
[7] Zhu Y, Sun Z, Yan Z, Jin Z, Tour JM. Rational design of hybrid graphene films for high-performance transparent electrodes. ACS Nano 2011;5(8):6472–9.
[8] Choi W, Lahiri I, Seelaboyina R, Kang YS. Synthesis of graphene and its applications: a review. Crit Rev Solid State Mater Sci 2010;35(1):52–71.
[9] Wu J, Agrawal M, Becerril HA, Bao Z, Liu Z, Chen Y, et al. Organic light-emitting diodes on solution-processed graphene transparent electrodes. ACS Nano 2009;4(1):43–8.
[10] Li H, Al-Aqtash N, Wang L, Qin R, Liu Q, Zheng J, et al. Electromechanical switch in metallic graphene nanoribbons via twisting. Physica E 2012;44(10):2021–6.
[11] Koskinen P. Graphene nanoribbons subject to gentle bends. Phys Rev B 2012;85(20):205429.
[12] Zang J, Ryu S, Pugno N, Wang Q, Tu Q, Buehler MJ, et al. Multifunctionality and control of the crumpling and unfolding of large-area graphene. Nat Mater 2013;12(4):321–5.
[13] Jiang T, Huang R, Zhu Y. Interfacial sliding and buckling of monolayer graphene on a stretchable substrate. Adv Funct Mater 2013.
[14] Gong L, Kinloch IA, Young RJ, Riaz I, Jalil R, Novoselov KS. Interfacial stress transfer in a graphene monolayer nanocomposite. Adv Mater 2010;22(24):2694–7.
[15] Gong L, Young RJ, Kinloch IA, Riaz I, Jalil R, Novoselov KS. Optimizing the reinforcement of polymer-based nanocomposites by graphene. ACS Nano 2012;6(3):2086–95.
[16] Ni ZH, Yu T, Lu YH, Wang YY, Feng YP, Shen ZX. Uniaxial strain on graphene: Raman spectroscopy study and band-gap opening. ACS Nano 2008;2(11):2301–5.
[17] Young RJ, Gong L, Kinloch IA, Riaz I, Jalil R, Novoselov KS. Strain mapping in a graphene monolayer nanocomposite. ACS Nano 2011;5(4):3079–84.
[18] Frank O, Tsoukleri G, Parthenios J, Papagelis K, Riaz I, Jalil R, et al. Compression behavior of single-layer graphenes. ACS Nano 2010;4(6):3131–8.

[19] Cranford SW. Buckling induced delamination of graphene composites through hybrid molecular modeling. Appl Phys Lett 2013;102(3):031902–31905.
[20] Reina A, Son H, Jiao L, Fan B, Dresselhaus MS, Liu Z, et al. Transferring and identification of single-and few-layer graphene on arbitrary substrates. J Phys Chem C 2008;112(46):17741–4.
[21] Gao Y, Li L, Tan P, Liu L, Zhang Z. Application of Raman spectroscopy in carbon nanotube-based polymer composites. Chin Sci Bull 2010;55(35):3978–88.
[22] Dresselhaus M, Dresselhaus G, Jorio A, Souza Filho A, Saito R. Raman spectroscopy on isolated single wall carbon nanotubes. Carbon 2002;40(12):2043–61.
[23] Ni Z, Wang H, Kasim J, Fan H, Yu T, Wu Y, et al. Graphene thickness determination using reflection and contrast spectroscopy. Nano Lett 2007;7(9):2758–63.
[24] Huang M, Yan H, Chen C, Song D, Heinz TF, Hone J. Phonon softening and crystallographic orientation of strained graphene studied by Raman spectroscopy. Proc Natl Acad Sci 2009;106(18):7304–8.
[25] Ferralis N. Probing mechanical properties of graphene with Raman spectroscopy. J Mater Sci 2010;45(19):5135–49.
[26] Geim AK, Novoselov KS. The rise of graphene. Nat Mater 2007;6(3):183–91.
[27] Kim KK, Reina A, Shi Y, Park H, Li L-J, Lee YH, et al. Enhancing the conductivity of transparent graphene films via doping. Nanotechnology 2010;21(28):285205.
[28] Gao Y, Li JZ, Liu LQ, Ma WJ, Zhou WY, Xie SS, et al. Axial compression of hierarchically structured carbon nanotube fiber embedded in epoxy. Adv Funct Mater 2010;20(21):3797–803.
[29] Seely FB, Smith JO. Advanced mechanics of materials. New York: Wiley; 1952.
[30] Yoon D, Son YW, Cheong H. Negative thermal expansion coefficient of graphene measured by Raman spectroscopy[J]. Nano Lett 2011;11(8):3227–31.
[31] Igeta M, Banerjee K, Wu G, et al. Thermal characteristics of submicron vias studied by scanning Joule expansion microscopy[J]. Electron Device Lett IEEE 2000;21(5):224–6.
[32] Griffiths SK, Crowell JAW, Kistler BL, et al. Dimensional errors in LIGA-produced metal structures due to thermal expansion and swelling of PMMA[J]. J Micromech Microeng 2004;14(11):1548.
[33] Calizo I, Balandin A, Bao W, Miao F, Lau C. Temperature dependence of the Raman spectra of graphene and graphene multilayers. Nano Lett 2007;7(9):2645–9.
[34] Tsoukleri G, Parthenios J, Papagelis K, Jalil R, Ferrari AC, Geim AK, et al. Subjecting a graphene monolayer to tension and compression. Small 2009;5(21):2397–402.
[35] Wortman J, Evans R. Young's modulus, shear modulus, and Poisson's ratio in silicon and germanium. J Appl Phys 2004;36(1):153–6.
[36] Lee DN. Elastic properties of thin films of cubic system. Thin Solid Films 2003;434(1):183–9.
[37] Ni ZH, Wang HM, Ma Y, Kasim J, Wu YH, Shen ZX. Tunable stress and controlled thickness modification in graphene by annealing. ACS Nano 2008;2(5):1033–9.
[38] Wu Q, Xu Y, Yao Z, Liu A, Shi G. Supercapacitors based on flexible graphene/polyaniline nanofiber composite films. ACS Nano 2010;4(4):1963–70.
[39] Timoshenko S, Gere JM. Theory of elastic stability. DoverPublications.com; 2012.
[40] Mei H, Huang R, Chung JY, Stafford CM, Yu H-H. Buckling modes of elastic thin films on elastic substrates. Appl Phys Lett 2007;90(15):151902–3.
[41] Mohiuddin T, Lombardo A, Nair R, Bonetti A, Savini G, Jalil R, et al. Uniaxial strain in graphene by Raman spectroscopy: G peak splitting, Grüneisen parameters, and sample orientation. Phys Rev B 2009;79(20):205433.
[42] Meyer JC, Geim A, Katsnelson M, Novoselov K, Booth T, Roth S. The structure of suspended graphene sheets. Nature 2007;446(7131):60–3.
[43] Fasolino A, Los J, Katsnelson MI. Intrinsic ripples in graphene. Nat Mater 2007;6(11):858–61.
[44] Lui CH, Liu L, Mak KF, Flynn GW, Heinz TF. Ultraflat graphene. Nature 2009;462(7271):339–41.
[45] Stolyarova E, Rim KT, Ryu S, Maultzsch J, Kim P, Brus LE, et al. High-resolution scanning tunneling microscopy imaging of mesoscopic graphene sheets on an insulating surface. Proc Natl Acad Sci 2007;104(22):9209–12.